Journal of Biomechanics 149 (2023) 111502

Contents lists available at ScienceDirect

Journal of Biomechanics

journal homepage: www.elsevier.com/locate/jbiomech

Pulse wave imaging of a stenotic artery model with plaque constituents of different stiffnesses: Experimental demonstration in phantoms and fluid-structure interaction simulation

Nima Mobadersany [a], Nirvedh H. Meshram [a], Paul Kemper [a], C.V. Sise [a], Grigorios M. Karageorgos [a], Pengcheng Liang [a], Gerard A. Ateshian [a,b], Elisa E. Konofagou [a,c,*]

[a] Department of Biomedical Engineering, Columbia University, New York, NY, United States
[b] Department of Mechanical Engineering, Columbia University, New York, NY, United States
[c] Department of Radiology, Columbia University, New York, New York, NY, United States

ARTICLE INFO

Keywords:
PVA phantom
Pulse wave velocity
Carotid plaque
Fluid–structure interaction simulation
Pulse wave imaging

ABSTRACT

Vulnerable plaques associated with softer components may rupture, releasing thrombotic emboli to smaller vessels in the brain, thus causing an ischemic stroke. Pulse Wave Imaging (PWI) is an ultrasound-based method that allows for pulse wave visualization while the regional pulse wave velocity (PWV) is mapped along the arterial wall to infer the underlying wall compliance. One potential application of PWI is the non-invasive estimation of plaque's mechanical properties for investigating its vulnerability. In this study, the accuracy of PWV estimation in stenotic vessels was investigated by computational simulation and PWI in validation phantoms to evaluate this modality for assessing future stroke risk. Polyvinyl alcohol (PVA) phantoms with plaque constituents of different stiffnesses were designed and constructed to emulate stenotic arteries in the experiment, and the novel fabrication process was described. Finite-element fluid–structure interaction simulations were performed in a stenotic phantom model that matched the geometry and parameters of the experiment in phantoms. The peak distension acceleration of the phantom wall was tracked to estimate PWV. PWVs of 2.57 ms^{-1}, 3.41 ms^{-1}, and 4.48 ms^{-1} were respectively obtained in the soft, intermediate, and stiff plaque material in phantoms during the experiment using PWI. PWVs of 2.10 ms^{-1}, 3.33 ms^{-1}, and 4.02 ms^{-1} were respectively found in the soft, intermediate, and stiff plaque material in the computational simulation. These results demonstrate that PWI can effectively distinguish the mechanical properties of plaque in phantoms as compared to computational simulation.

1. Introduction

Pulse waves are pressure waves generated by the heart's left ventricle during each contraction phase propagating throughout the arterial tree (Nichols et al., 2011). Pulse wave velocity (PWV) is linked to arterial stiffness, and it is a strong predictor of cardiovascular diseases in hypertensive patients (Blacher et al., 2001), arteriosclerosis (Liu et al., 2007), cognitive impairment (Scuteri and Wang, 2014), end-stage renal disease (Blacher et al., 2003), coronary artery atherosclerosis (Chiha et al., 2016; Kim et al., 2018; Lim et al., 2004), cerebral artery atherosclerosis (Zhai et al., 2018), and carotid artery atherosclerosis (Kim and Kim, 2019; Zureik et al., 2002).

Pulse Wave Imaging (PWI) is a non-invasive ultrasound-based method that estimates regional pulse wave velocity (PWV) along the artery to assess underlying wall compliance (Apostolakis et al., 2017; Couade et al., 2011; Fujikura et al., 2007; Karageorgos et al., 2022, 2021; Vappou et al., 2010). One potential application of the PWI method is the non-invasive assessment of the mechanical properties of atherosclerotic plaque in the common carotid artery.

Stroke, the leading cause of disability in adults and one of the most common causes of death worldwide, is mainly caused by atherosclerotic plaque rupture leading to blockages downstream in the brain (Cicha et al., 2011; Donnan et al., 2008). Unstable plaques characterized by the combination of a large lipid core covered by a thin fibrous cap are

* Corresponding author at: Columbia University, Department of Biomedical Engineering, 351 Engineering Terrace, 1210 Amsterdam Avenue, New York, NY 10027, United States.
E-mail address: ek2191@columbia.edu (E.E. Konofagou).

https://doi.org/10.1016/j.jbiomech.2023.111502
Accepted 13 February 2023
Available online 17 February 2023

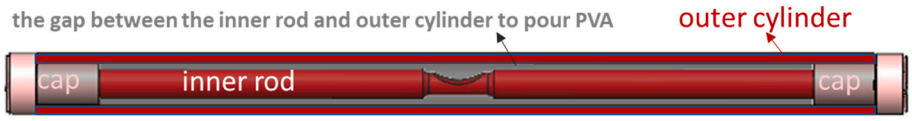

Fig. 1. Schematic of the molds. The molds consisted of an inner rod that occupied the negative cavity representative of the lumen and a hollow outer cylinder that would determine the thickness of the phantom wall. The molds were filled with PVA solution, and the ends were sealed with caps to avoid dehydration due to contact with air. The molds were then exposed to repeated freezing and thawing cycles (12 hrs. / cycle) that solidifies and generates PVA phantoms where the number of cycles determined the stiffness.

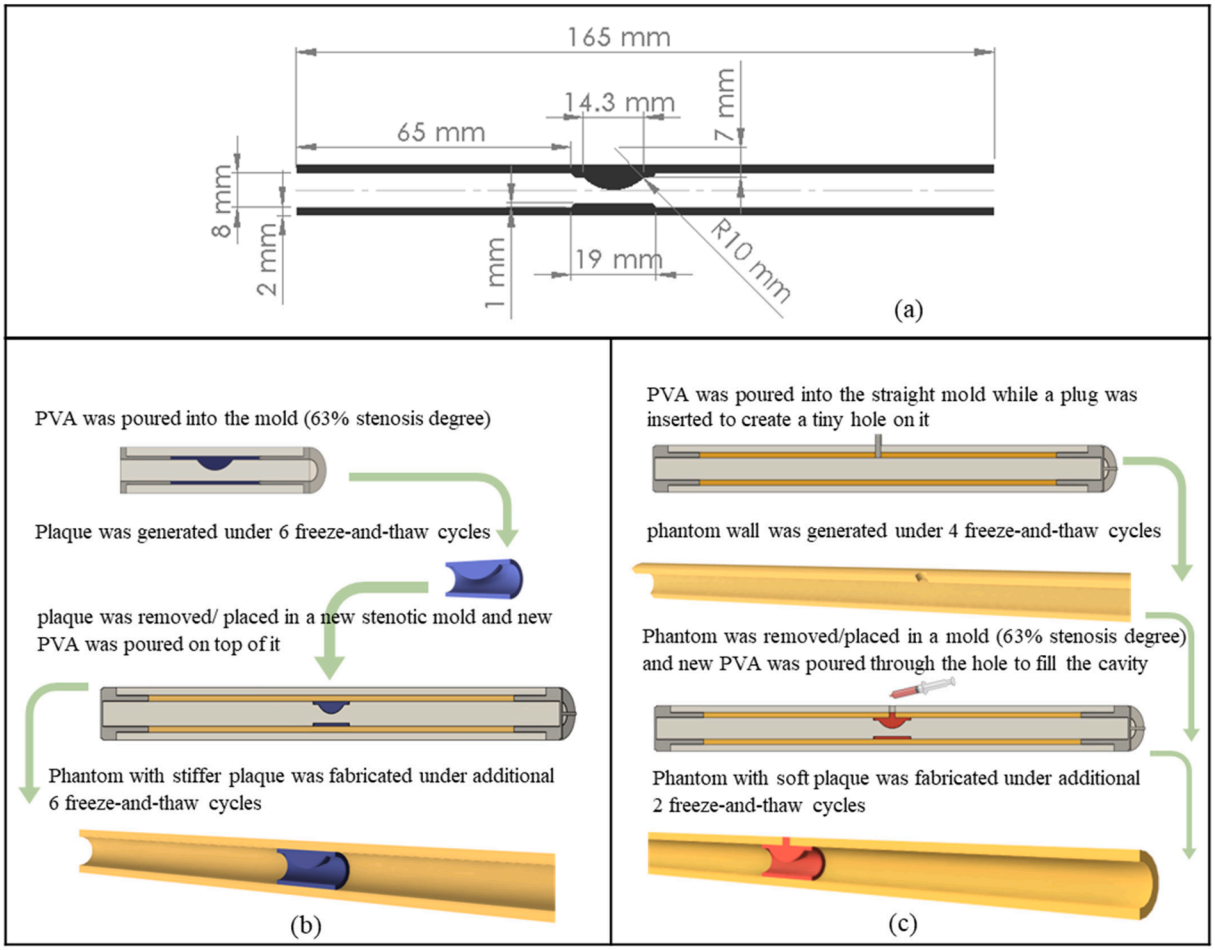

Fig. 2. (a) Planar view of the stenotic phantom at the longitudinal section. All the phantoms in this study have the same geometry. The plaque was modeled as a spherical occlusion attached to a 1 mm-thick wall with 19 mm length extruding from the inner surface of the phantom wall starting 65 mm longitudinally from the inlet of the artery model. The occlusion was generated by symmetric, circumferential plaque revolving around a 14.3 mm-long longitudinal segment at the inner wall surface. The circumferential plaque has a radius of 10 mm and is centered at 7 mm from the inner wall surface. A 1 mm-thick wall was necessary to build the stiff plaque so that the plaque would hold onto the inner rod at the stenosis as we needed to pour a new PVA solution on top of it to make the phantom wall. However, the 1 mm-thick wall was maintained in the intermediate and soft plaques as well for the consistency in the phantom geometry throughout the study, (b-c) Fabrication process of the PVA phantom with stiff and soft plaque respectively.

vulnerable to rupture (Hafiane, 2019; Saba et al., 2014). Therefore, plaque composition may provide valuable information on the risk for rupture, as it can assist clinicians in their intervention strategy.

The feasibility of Pulse Wave Imaging in atherosclerotic plaque characterization has been assessed in the human carotid artery through qualitative observation of elevated pulse wave velocity and decreased displacement within atherosclerotic plaque (Li et al., 2019) and arterial wall inhomogeneity (Karageorgos et al., 2020). Along with PWI, other imaging modalities (e.g., Magnetic Resonance Imaging, Computed Tomography), as well as several ultrasound-based techniques, have also been developed for assessing the mechanical properties of plaques (Czernuszewicz et al., 2015; Lechareas et al., 2016; Majdouline et al., 2014; Marlevi et al., 2020; Widman et al., 2015; Wu et al., 2021).

In addition, several studies investigated the effect of material properties and structure of carotid atherosclerotic plaque on stress distribution and hemodynamic shear stress for plaque vulnerability using fluid–structure interaction (FSI) simulations (Ahmadi and Ansari, 2019; Bennati et al., 2021; Patel et al., 2021; Tang et al., 2005; Wong et al., 2012; Yuan et al., 2015; Zhou et al., 2017).

Pulse wave velocity is correlated with the elastic modulus of the arterial wall through Moens- Korteweg analytical equation, $PWV = \sqrt{Eh/(2\rho R(1-\vartheta^2))}$, where E is Young's modulus of the vessel wall, h is the vessel wall thickness, R is the vessel radius, ρ is the blood density, and ϑ is the Poisson's ratio of the vessel wall. The equation holds for a purely elastic infinite straight cylindrical tube having small

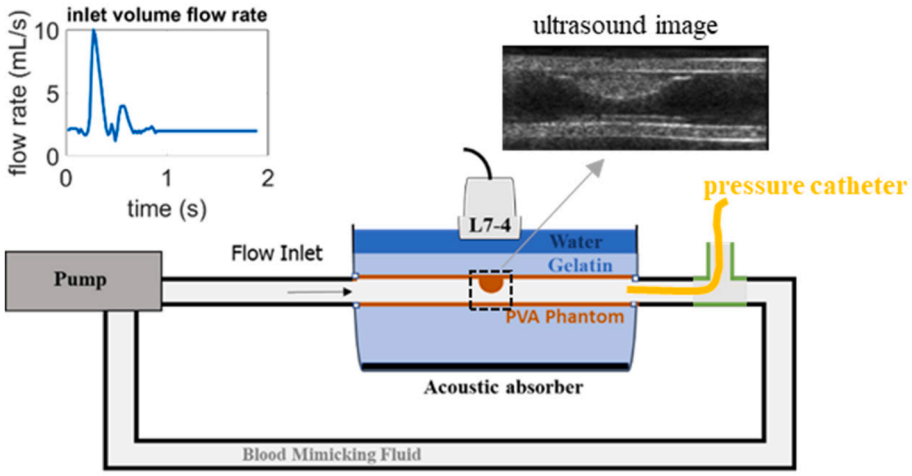

Fig. 3. Schematic of the experiment setup and ultrasound acquisition.

deformations and filled with an incompressible fluid. However, the correlation of the PWV with stiffness in stenotic vessels is complex and requires computational simulations.

several studies utilized FSI simulations for studying pulse wave propagation and PWV; i.e. in a fluid-filled elastic tube (Bazilevs et al., 2006), and straight arterial models (Elkenani et al., 2017; Shahmirzadi et al., 2012). The feasibility of an FSI-based computational approach in developing PWI methods using the open-source finite element software FEBio has been previously examined for an ideal stenotic arterial model with a plaque of identical material properties as the wall (Gatti et al., 2020; Shim et al., 2021). In this study, the accuracy of regional PWV estimation in stenotic vessels with plaque constituents of different materials was further investigated in phantoms using PWI. For the experiment, PVA phantoms with plaque constituents of different stiffnesses were designed and constructed using computer-aided design (CAD) tools and 3D printing, using a novel fabrication process described in the paper. In addition, FE-FSI simulations were employed on the stenotic phantom models to investigate the accuracy of FSI-based computational simulation in predicting the variations in PWV in different plaque constituents by verifying them with PWI in validation phantoms. So that the simulation could support further development of PWI methods in characterizing plaque vulnerability and clinical findings in future studies.

Because of the changes in the geometry, and the fluid pressure along the stenosis, PWVs would continuously vary at the plaque. However, PWVs in this study are assumed constant along each segment (pre-stenosis/stenosis/post-stenosis) which was found by fitting a linear regression line between the time points of the arrival of the wave of the peak distension acceleration and the corresponding locations. Further work will exploit this framework to assess the sensitivity of PWI to detect small changes of interest in combination with the geometry change.

2. Methods

2.1. Constructing Polyvinyl alcohol arterial mimicking phantom

Stenotic PVA phantoms with 63% ± 5% degree of stenosis (the maximum percentage of the arterial wall inner diameter occluded by the stenosis) were designed to mimic the arterial wall with plaque constituents of different stiffnesses: soft, intermediate, and stiff. For this purpose, molds were designed and constructed using CAD modeling (Solidworks, Dassault systems, Vélizy-Villacoublay, France) and 3D printing (Formlabs, Massachusetts, USA), as shown in Fig. 1.

The PVA solution consisted of deionized water (78% fractional weight), PVA powder (Sigma-Aldrich, St. Louis, MO) to form viscoelastic walls (10% fractional weight), glycerol to increase the sound speed (10% fractional weight), and graphite acoustic scatters (Sigma-Aldrich, St. Louis, MO) with 3% fractional weight. The solution was mixed at 90 °C until fully homogenized, after which it was left to cool and degassed (Chayer et al., 2019; Chee et al., 2016; Galluzzo et al., 2015; Gatti et al., 2020). In addition, the PVA solution used for forming the plaques was poured into 1 cm cubes following the exact freeze-and-thaw cycle process. These cubes were then used for mechanical testing to find material characteristics of plaques and phantom wall. Fig. 2(a) illustrates the schematic of the stenotic phantom.

For constructing the phantom with stiff plaque (Fig. 2(b)), the PVA solution was poured into a stenotic mold and was exposed to six freeze-and-thaw cycles, after which it was removed from the mold. The edges of the newly built stenotic phantom were cut and removed so that a small stenotic section (Plaque) was left, which was subsequently put back in the mold by slowly sliding it in. The mold was then filled with a new PVA solution to create the phantom wall with a thickness of 2 mm. The mold was then exposed to six more repeated freeze-and-thaw cycles. Thus, the plaque and the phantom wall experienced twelve and six freeze-and-thaw cycles, respectively, so we could achieve stiffer plaque in the middle of the artery model while the rest of the phantom had lower stiffness.

For the phantom with soft plaque (Fig. 2(c)), we followed a different procedure by forming the phantom wall first. For this purpose, the PVA solution was filled into a mold with an outer cylinder and an inner straight rod (no cavity) to generate a straight phantom. A plug was also placed in the middle section of the outer cylinder mold to create a phantom with a small hole crossing through the phantom wall. The solution was then exposed to four freeze-and-thaw cycles, after which it was removed from the mold. The straight phantom was put back into a mold with a stenotic rod. Then a new PVA material was injected through the small hole of the straight phantom to fill the cavity. The mold was then exposed to two more freeze-and-thaw cycles. Thus, the plaque and the phantom wall experienced two and six freeze-and-thaw cycles, respectively, so we could achieve softer plaque in the middle of the artery model.

For the phantom with intermediate plaque, the PVA solution was poured into the mold having an inner rod with a cavity. The PVA solution was exposed to six freeze-and-thaw cycles to generate a stenotic phantom where the plaque and the phantom wall has similar material property.

Finally, all three phantoms were removed from the molds and mounted onto a custom-made box through fittings placed in the box. The fittings were built using CAD models and 3D-printed. The fittings were extruded about 10 cm from the box to establish a fully developed flow in

Table 1
Material mechanical properties.

Material	Elastic constants (Ogden first order)		Viscoelastic constants		Young's modulus at the limit of zero strain (from the stiffness matrix of the Ogden material)
	c	m	γ	τ	$E_0(kPa)$
Softer Plaque	7842	−3.1	0.055	1500	12
Wall & intermediate plaque	17,389	−8.7	0.139	1498	30
Stiffer Plaque	52,500	−1.19	0.202	1500	95

The gelatin was modeled as a homogenous isotropic compressible quasi-linear viscoelastic material (Gatti et al., 2020) with a neo-Hookean equilibrium elastic response ($E = 5.98$ kPa, Poisson's ratio $\upsilon = 0.41$, $\gamma = 0.37$, $\tau = 1044$ s)

the phantom. To prepare and mimic the tissue around the phantoms, porcine-skin gelatin (Sigma-Aldrich, St. Louis, MO) with a fractional weight of 4% was added in hot deionized water, and the solution was boiled to let thoroughly mix. The gelatin solution was then poured into the box around the phantoms once it is cooled to room temperature and degassed. The box was placed back in the fridge (4 °C) for two days before the experiment to let the gelatin solidify. Also, before pouring the gelatin, the phantoms were filled with deionized water and sealed so they would not dehydrate and collapse in the fridge.

2.2. Flow experiment and pulse wave Imaging

A computer-controlled displacement pump (CompuFlow 1000, Shelley Medical Imaging Technologies, Toronto, Canada) was connected to the inlet and outlet of the phantom to circulate blood-mimicking fluid (Ramnarine et al., 1998). The pump generated a physiological pulsatile flow with a waveform like that in the common carotid artery (Holdsworth et al., 1999) with an amplitude of 10 mL/s as illustrated in Fig. 3. The total duration of 1.9 s was set for each pump cycle. Each cycle included a 0.9 s of a common carotid artery flow waveform followed by a 1 s interval to allow the attenuation of the reflections from the previous cycle before the beginning of a new cycle and eliminate the effect of reflected waves from the previous cycle in the forward wave of the new cycle. The pulse wave propagation was tracked over the phantom by monitoring the distension of the phantom wall within a single cycle using the Pulse Wave Imaging technique. An L7-4 Linear array transducer with 128 elements, a center frequency of 5.2 MHz, and 60% Bandwidth (L7-4, ATL Ultrasound, Bothell, WA, USA), was connected to a Verasonics Vantage 256 research platform (Verasonics, Bothell, WA, USA). The probe was mounted on a computer-controlled motorized translation stage that could be shifted along the phantom to acquire signals over the phantom width in three steps, one every 37.8 mm corresponding to the field of view of L7-4. To quantify the PWV, the peak of the distension acceleration waveform was tracked across the field of view of the propagation on the spatiotemporal map to estimate pulse wave arrival time (for more details Appendix A).

2.3. Material properties

The PVA material was modeled as a homogeneous isotropic nearly incompressible quasilinear viscoelastic material (Gatti et al., 2020). The non-linear elastic behavior of the material was defined using a first-order hyperplastic Ogden model. The Ogden material is expressed using the following hyperplastic strain energy function, $W = (c/m^2)\left(\tilde{\lambda}_1^m + \tilde{\lambda}_2^m + \tilde{\lambda}_3^m - 3\right)$ where $\tilde{\lambda}_i$ are the deviatoric principal

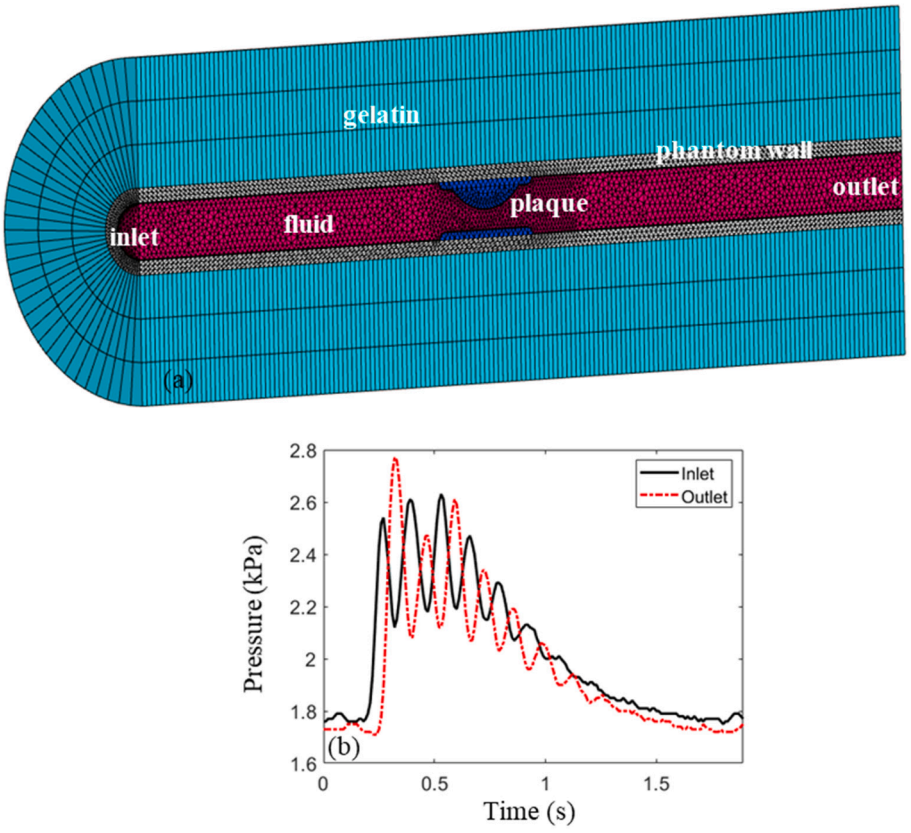

Fig. 4. (a) Axonometric view of the geometry and mesh of the finite element model with the dimensions matching the experiment, (b) pressure boundary conditions at the inlet and outlet of the fluid domain for FSI simulation.

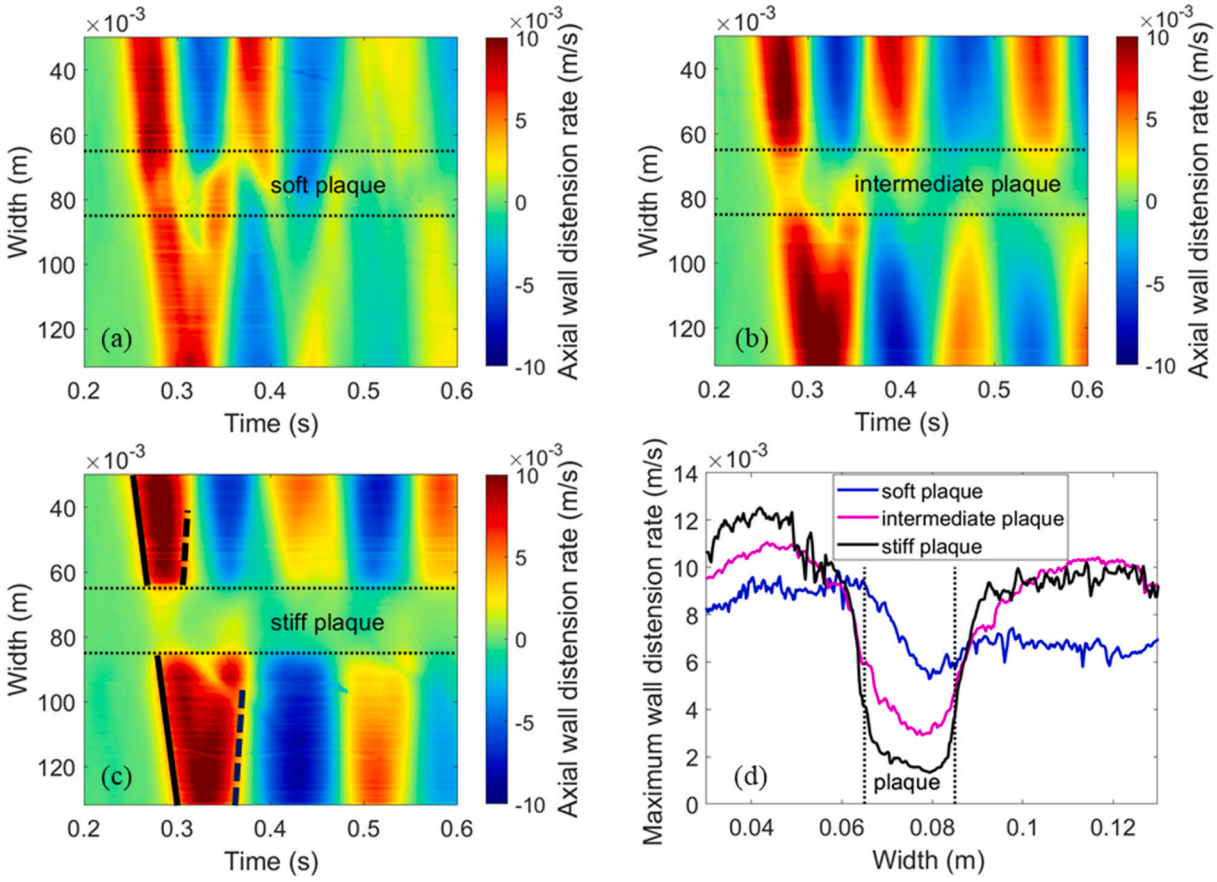

Fig. 5. Spatiotemporal maps of the axial wall distension rate along the phantom with (a) soft plaque, (b) intermediate plaque, (c) stiff plaque in the experiment using PWI, and (d) maximum axial wall distension rate along the phantom. Thin-dashed lines represent the boundaries of the stenosis. The forward wave (the first red front with a positive slope) and the reflected wave (the first red front with a negative slope) are respectively shown with the solid and thick-dashed lines at the pre-stenosis and post-stenosis in Fig. 5(c) for more clarification. Note that the reflection from the phantom outlet is more visible compared to the reflection at the plaque. This could be because of the stronger impedance mismatch between the phantom and the container compared to that between the pre-stenosis and the plaque, as well as the longer distance of the phantom outlet from the plaque which allows more separation time between the forward wave and reflected wave from the phantom outlet. (For interpretation of the references to colour in this figure legend, the reader is referred to the web version of this article.)

stretches, and c and m are elastic material parameters. An exponential relaxation function of the form $G(t) = 1 + \gamma e^{(-t/\tau)}$ was used to model the quasilinear viscoelastic behavior of the material, where $1 + \gamma$ represents the ratio of instantaneous to equilibrium modulus and τ is the relaxation time constant. The material properties (c, m, γ, and τ) were extracted by fitting the viscoelastic material model using the Levenberg-Marquardt method within the FEBio finite element software (Maas et al., 2012) to the unconfined compression stress-relaxation test data (for more details Appendix B). These properties were then used in the phantom wall and plaque models in the FSI simulations (Table 1).

2.4. Fluid-Structure interaction (FSI) simulation

The propagation of a pulse wave was simulated using finite element-based fluid–structure interaction simulations (FE-FSI) in FEBio (Maas et al., 2012; Shim et al., 2019). For the simulation, the 3D CAD model of the phantom was first built and meshed in Abaqus CAE (Dassault systems, Vélizy-Villacoublay, France), as illustrated in Fig. 4 (a). The CAD model consisted of the stenotic phantom built with the same geometry used in the experiment and a surrounding 24 mm-thick gelatin sleeve. Due to the symmetry about the longitudinal plane, only half of the model was constructed for the simulation to reduce computational costs. The fluid domain, the phantom wall, and the plaque meshed with quadratic tetrahedral elements with a maximum node-to-node distance of 1 mm, and the gelatin meshed with quadratic hexahedral elements. The mesh at the phantom wall and at the fluid in the stenotic region was customized and refined. To capture the boundary layer effects, a 0.16 mm thick boundary layer mesh was applied at the interface of the phantom and fluid flow using quadratic wedge elements.

The simulations were run in FEBio over two analysis steps, including a first step which increased the flow pressure to that in the experiment in phantoms, followed by a second step that ran for 0.6 s with a maximum time step of *1* ms to ensure proper accuracy in the time domain. For details on the FSI implementation, please see (Shim et al., 2019). The blood-like fluid constituent in the fluid-FSI domain was simulated as a slightly compressible Newtonian viscous fluid with a shear viscosity of 0.004 Pa.s, mass density of 1060 kg.m^{-3}, and bulk modulus of 2.2 GPa. The solid constituent in the fluid-FSI domain was modeled as a massless compressible neo-Hookean elastic solid with a very low Young's modulus (1 nPa) and zero Poisson's ratio. Zero displacement was prescribed as the boundary condition on the outer wall of the gelatin, at the inlet and outlet faces of the phantom, and on the mesh of the fluid-FSI domain at the inlet and outlet faces. Zero normal displacement was applied on the symmetry plane for these same domains. No-slip boundary and fluid-FSI traction were prescribed at the interface of the fluid-FSI domain and the inner wall of the phantom. Pressure boundary conditions were prescribed at the inlet and outlet of the fluid domain. Inlet and outlet pressures were obtained from experimental measurements using a Mikro-Tip pressure catheter (MPR-500, Miller, Houston, TX) where a three-way tube was added to the phantom allowing the catheter to be inserted into the phantom. Before pressure measurements,

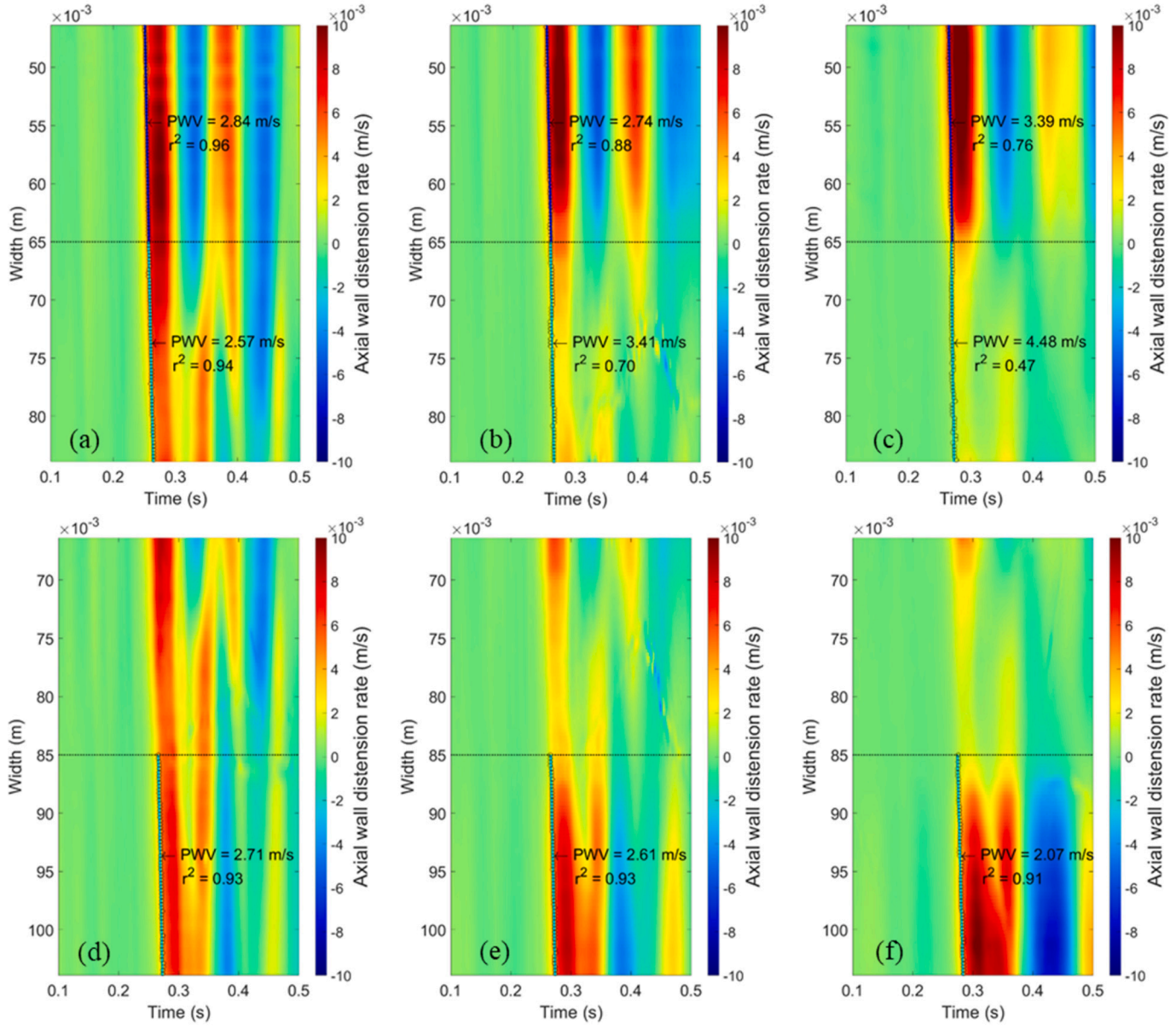

Fig. 6. PWVs at the pre-stenosis, stenosis, and post-stenosis of the phantom with (a, d) soft plaque, (b, e) intermediate plaque, (c, f) stiff plaque in the experiment using PWI. The small circles overlaid on the spatiotemporal maps indicate the arrival time of the peak distension acceleration. A linear regression line was fitted to the map between the time-points of arrival of the wave of the peak acceleration and the corresponding locations representative of the traveled distance. The slope of the linear fit estimated the PWV with a coefficient of determination r^2 indicative of the precision of the fit. Dashed lines represent the boundaries of the stenosis. The PWV was measured over segments with around 19 mm width corresponding to half of the distance over the field of view and the approximate width of the plaque.

the catheter was calibrated by a transducer calibration device (Delta-Cal, Utah Medical Products, Midvale, Utah). The signals received from the catheter were then converted to pressures (Fig. 4(b)). The pressure values show fluctuations which could be the consequence of pulse wave reflections, and turbulence due to the nature of the setup and the pump.

3. Results

Figure 5(a-c) shows the spatiotemporal maps of the axial distension rate of the three phantoms with plaque constituents of different stiffnesses: soft, intermediate, and stiff during the experiment using PWI. As it is seen in the spatiotemporal map of the wall distension rate, the pulse peak arrives at the phantom at around t = 0.25 s. The pulse wave then propagates along the phantom wall and gets reflected at the plaque and phantom outlet. Due to the nature of the phantom experiment where the phantom is mounted and tied to the fittings of the box, significant reflections occur which reverberate along the phantom. Note that the reflection at the plaque appears in the first red front with a negative slope at the pre-stenosis around t = 0.3 s (i.e., thick-dashed line in Fig. 5(c)). However, the reflected wave is merged with the forward wave, making it visually difficult to separate. This reflection is more noticeable in the stiff plaque (Fig. 5(c)) compared that in the soft plaque (Fig. 5(a)).

Fig. 5(d) shows the maximum axial wall distension rate for those three phantoms. As expected, the axial wall distension rate in stiff plaque had the smallest value among these three plaque constituents. As observed in Fig. 5(a-d), the phantom wall had a much lower axial distension rate at the stenosis due to lower circumferential stress. Fig. 6 shows the pulse wave velocity obtained from PWI at the stenotic region of the phantoms with soft plaque, intermediate plaque, and stiff plaque.

Figure 6(a-c) shows the pulse wave velocity at the pre-stenosis and stenosis, and Fig. 6(d-f) at the post-stenosis of the phantoms. PWVs were mapped on the spatiotemporal map of the axial wall distension rate.

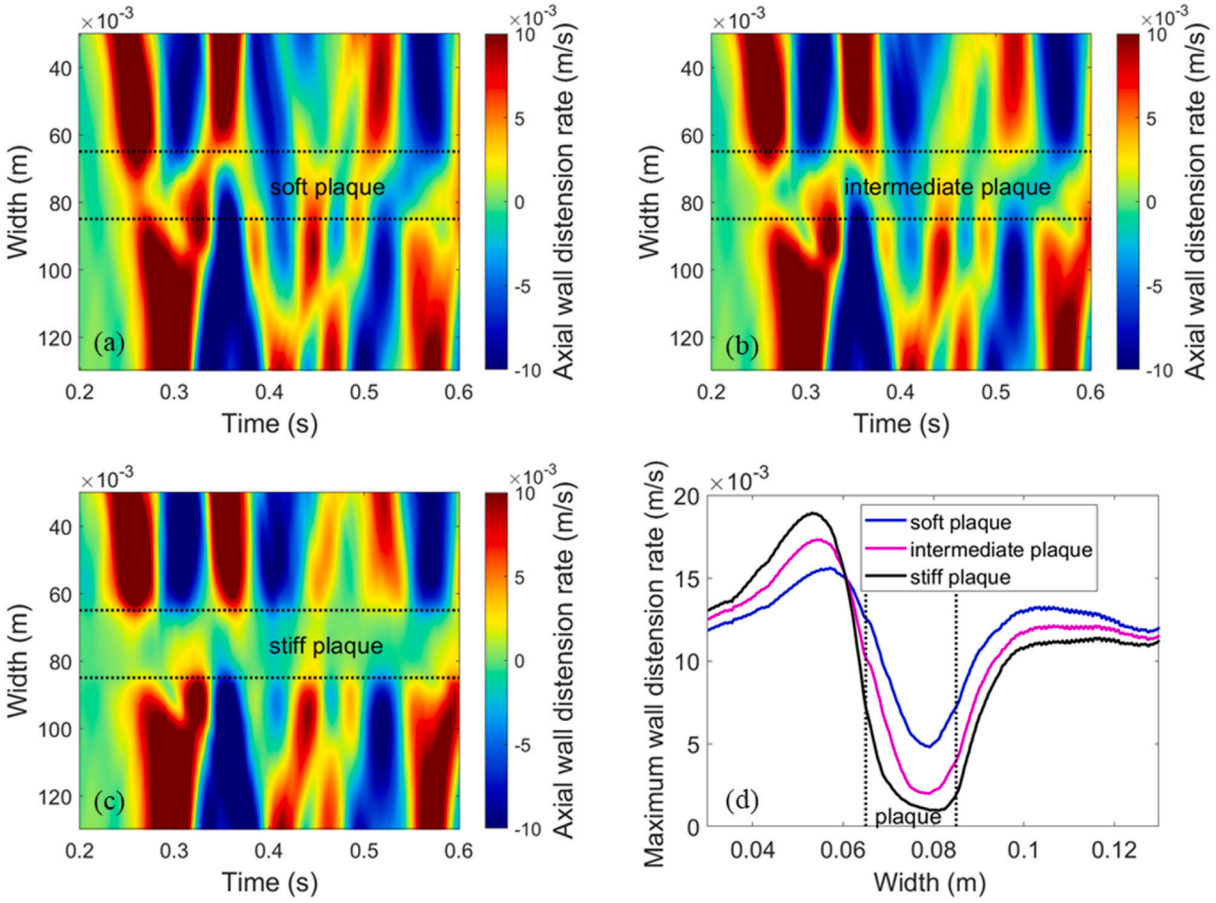

Fig. 7. Spatiotemporal maps of the axial wall distension rate along the phantom with (a) soft plaque, (b) intermediate plaque, (c) stiff plaque in the FSI simulation. (d) maximum axial wall distension rate along the phantom. Dashed lines represent the boundaries of the stenosis.

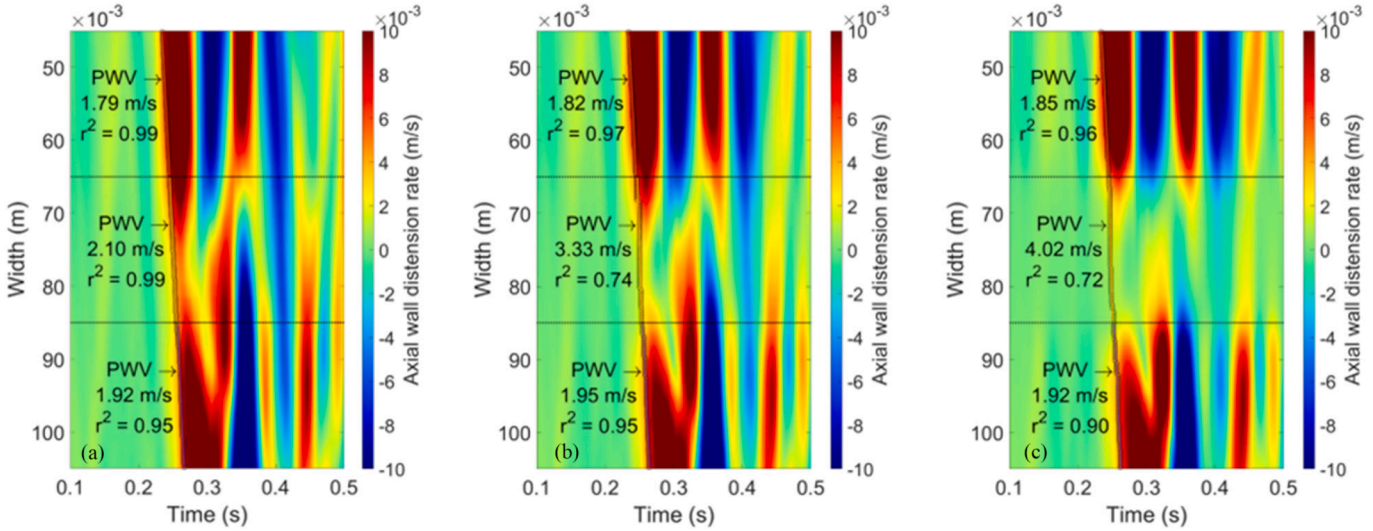

Fig. 8. PWVs at the pre-stenosis, stenosis, and post-stenosis of the phantom with (a) soft plaque, (b) intermediate plaque, (c) stiff plaque in the FSI simulation. The small circles overlaid on the spatiotemporal maps indicate the arrival time of the peak distension acceleration. A linear regression line was fitted to the map between the time points of the arrival of the wave of the peak acceleration and the corresponding locations representative of the traveled distance. The slope of the linear fit estimated the PWV with a coefficient of determination r^2 indicative of the precision of the fit. Dashed lines represent the boundaries of the stenosis. The PWV was measured over segments with around 19 mm width corresponding to half of the distance over the field of view and the approximate width of the plaque.

Peak acceleration of the wall distension waveform was tracked to find the pulse wave arrival time since it provided better separation (less interference) between the forward and reflected wave at the stenosis for more accurate estimation of the pulse wave arrival time (for more details Appendix C). The RF data were acquired such that the boundary of the stenosis and phantom wall lies under the middle of the field of view so

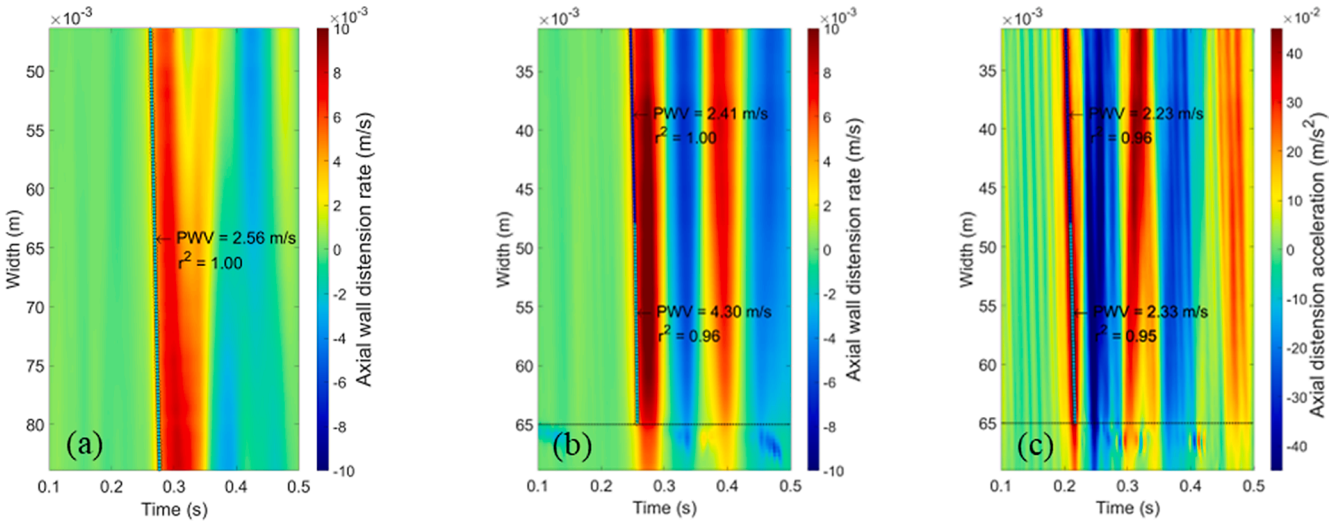

Fig. C1. Experimental data of the spatiotemporal maps from PWI and PWV (a) in the straight phantom with 50% upstroke of velocity waveform arrival time marker, (b) in the pre-stenosis of the stenotic phantom with 50% upstroke of the velocity waveform arrival time marker, (c) in the pre-stenosis of the stenotic phantom with the peak acceleration of the waveform arrival time marker. The small circles overlaid on the maps indicate the marker arrival time with the corresponding linear fitting. Dashed lines indicate the boundary of the stenosis.

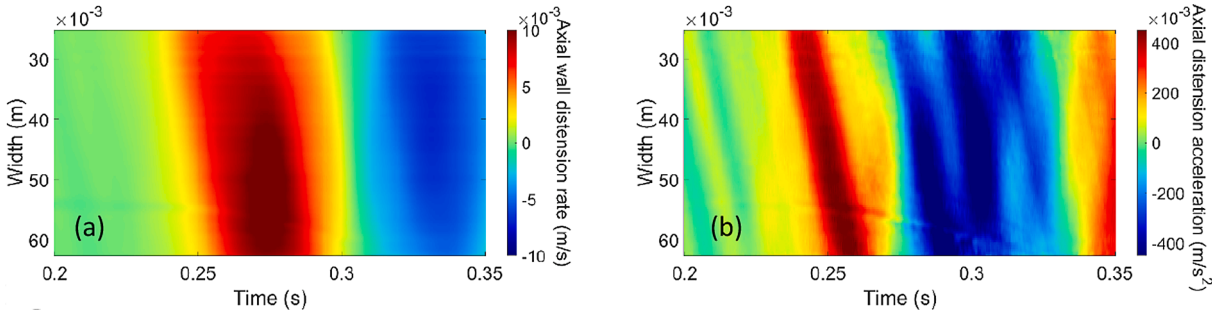

Fig. C2. Experimental data of the spatiotemporal map of (a) axial wall distension rate, (b) axial wall distension acceleration at the pre-stenosis of the stenotic phantom using PWI.

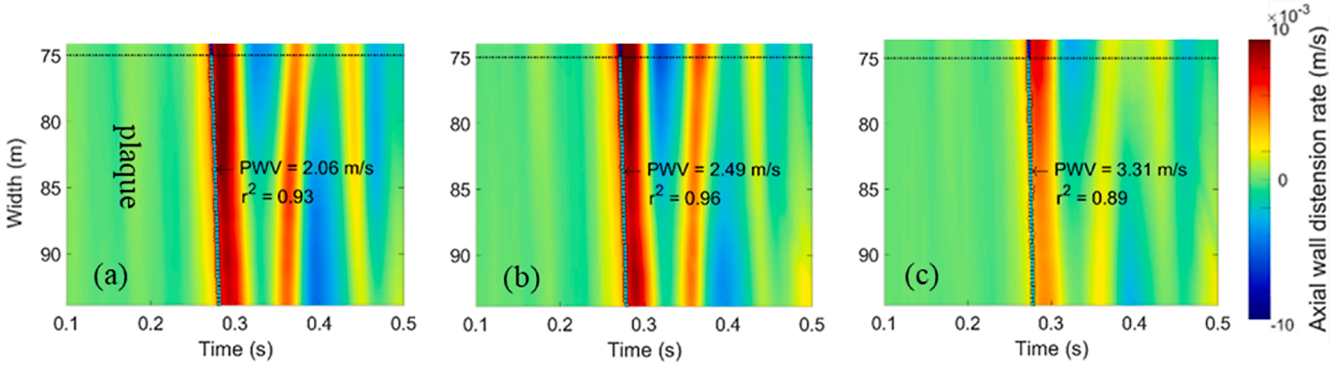

Fig. D1. Spatiotemporal map of the wall distension rate and PWV at the stenosis of three PVA phantoms (50% stenosis degree) with (a) soft plaque, (b) intermediate plaque, and (c) stiff plaque. The mechanical properties and stiffness of these phantoms are different from those discussed earlier throughout this study A linear regression line was fitted to the spatiotemporal map between the time points of the arrival of the peak acceleration waveform and the corresponding locations representative of the traveled distance. The slope of the linear fit estimated the PWV with a coefficient of determination r^2 indicative of the goodness of the fit.

that PWV is mapped over equally distanced segments at the pre-stenosis, stenosis, and post-stenosis for consistency. Due to the changes in the geometry and the pressure along the stenosis, PWVs would continuously vary at the plaque. However, PWVs in this study are assumed constant at each segment which was found by fitting a linear regression line between the time points of the arrival of the wave of the peak distension acceleration and the corresponding locations representative of the traveled distance in that segment with the coefficient of determination r^2 indicative of the goodness of the linear fit. The pulse wave velocity values at the plaque were reported in the following with the 95% confidence bounds associated with the linear fit.

Pulse wave velocities of 2.57 ms^{-1} (95% confidence interval of the

PWV: 2.41 ms^{-1} to 2.70 ms^{-1}), 3.41 ms^{-1} (95% confidence interval of the PWV: 2.95 ms^{-1} to 4.21 ms^{-1}), and 4.48 ms^{-1} (95% confidence interval of the PWV: 4.13 ms^{-1} to 7.67 ms^{-1}) were found in the phantom experiment using PWI for soft plaque, intermediate plaque, and stiff plaque respectively. Also, PWVs of 2.84 ms^{-1}, 2.74 ms^{-1}, and 3.39 ms^{-1} were found, respectively, at the pre-stenosis of the phantoms with soft, intermediate, and stiff plaques. Due to larger reflection, higher PWV was estimated at the pre-stenosis of the phantom with a stiff plaque compared to those in the phantoms with soft and intermediate plaques even though the wall material is similar for all the phantoms.

Figure 7 (a-c) shows the pulse wave propagation on the three studied phantoms in FSI simulations visualized as the spatiotemporal map of phantom wall distension rate, and Fig. 7(d) shows the corresponding maximum wall distension rate along the phantom wall. Overall good agreement is observed for pulse wave propagation between phantom experiments using PWI (Fig. 5) and FSI simulation (Fig. 7). However, the phantom wall had a larger distension rate in FSI simulations compared to experiments.

Fig. 8 shows the corresponding pulse wave velocity at pre-stenosis, stenosis, and post-stenosis in FSI simulations using peak distension acceleration arrival time marker. Similar to the experiment in phantoms, PWVs were mapped on the spatiotemporal map of the axial wall distension rate. PWVs of 2.10 ms^{-1}(95% confidence interval of the PWV: 2.04 ms^{-1} to 2.16 ms^{-1}), 3.33 ms^{-1}(95% confidence interval of the PWV: 2.88 ms^{-1} to 3.94 ms^{-1}), and 4.02 ms^{-1} (95% confidence interval of the PWV: 3.46 ms^{-1} to 4.80 ms^{-1}) were found in the FSI simulations for soft plaque, intermediate plaque, and stiff plaque constituents respectively. Also, PWV of around 1.8 ms^{-1} was found at the pre-stenosis in the simulation. FSI simulations were able to quantify larger PWV values for stiffer plaques. However, the predicted PWVs at the stenotic region in the FSI simulations were lower than those in the phantom experiments. It is worth mentioning that we also performed a similar experiment in a different set of constructed phantoms and found consistent results with the results of the current study where PWI could quantify larger PWV with the increase of stiff material content in the plaque (for more details Appendix D).

4. Discussion

The objective of the current study was to investigate pulse wave propagation on stenotic artery models with plaque constituents of different stiffnesses to find the regional pulse wave velocity in the stenotic region with the PWI method for assessing plaque vulnerability. Therefore, PVA phantoms with stiff, soft, and intermediate plaques were designed and the novel fabrication process was demonstrated. FSI simulations were performed to verify that variations in plaque stiffness produce variations in PWV that are consistent with experimental observations so that computational simulations could serve as an alternative for developing PWI methods and supporting clinical findings. The FSI simulations and phantom experiments using PWI showed good agreement in quantifying the plaque compliance based on the PWV, with a stiffer plaque showing a larger PWV in both cases. Relative errors of 18%, 2.3%, and 10% were observed in PWVs between the phantom experiment and FSI simulation for soft plaque, intermediate plaque, and stiff plaque, respectively. However, FSI simulations predicted lower PWVs at the stenotic region and larger distension rates compared to those in phantom experiments, though trends were similar. Comparing the PWVs at the pre-stenosis region between the phantom experiments and FSI simulations showed relative errors of 37%, 33%, and 45% in PWVs at the pre-stenosis in the phantoms with soft plaque, intermediate plaque, and stiff plaque, respectively.

Pulse wave velocity is associated with blood flow pressure (Spronck et al., 2015). Therefore, the difference observed in PWVs may be attributed to the inaccuracy in pressure measurement at the phantom outlet during experiments since those were later used in the FSI simulations. Downstream of the plaque, vortices were generated that traveled along the phantom due to vortex shedding. The Reynolds number of the flow in this study was *423* (maximum flow velocity of 0.2 m/s at the upstream of the plaque, characteristic length (lumen diameter) = 8×10^{-3} m, and kinematic viscosity of fluid = 3.78×10^{-6} m^2/s) which is in the laminar regime. However, laminar flow does not prevent vortex shedding (Bluestein et al., 1999; Paley et al., 2000); therefore the flow may become disturbed downstream of the plaque. Given the length of the phantom in our experiment, shedded vortices most likely did not dissipate entirely at the phantom outlet. This may have caused inaccuracies in the pressure readings, as the pressure may have fluctuated significantly along the lumen cross-section.

Inaccuracy in estimating mechanical properties could also induce differences between FSI simulations and phantom experiments. Comparing the PWV values and wall distension rates between phantom experiments and FSI simulations suggests that the mechanical stiffness may have been underestimated in FSI simulations, behaving as though they were softer than that in the phantom experiments. PVA phantoms have the advantage of providing artery-like vessel elasticity, high acoustic compatibility, and readily tunable mechanical properties (Chee et al., 2016; Surry et al., 2004); however, their mechanical properties are time-sensitive (Gatti et al., 2020).

Given these potential experimental limitations, it is essential to emphasize that exact agreement between FSI simulations and phantom measurements was not required for the primary aim of this study. We aimed to demonstrate that PWV could detect significant differences in plaque stiffness, as simulated experimentally with these phantoms, and that the variations in PWV with plaque stiffness would be consistent with predictions from FSI simulations. In this context, our aim was achieved successfully, with a highly satisfactory agreement between these two methods.

5. Conclusion

This study investigates pulse wave propagation in stenotic phantoms with plaque constituents of different stiffnesses using Pulse Wave Imaging and validated against FSI simulations. The objective of this study was to evaluate the ability of PWI to measure regional pulse wave velocity in pre-stenosis, stenosis, and post-stenosis regions, for ischemic stroke risk assessment. PVA phantoms with plaque constituents of different stiffnesses were designed for the experiment, and a novel fabrication process was described. The number of freeze-and-thaw cycles modulated the plaque stiffness during the fabrication process. Stenotic phantoms with three different plaque constituents; soft (E_0 = 12 kPa), intermediate (E_0 = 30 kPa), and stiff (E_0 = 95 kPa) were investigated throughout the study, where E_0 is the equilibrium Young's modulus in the limit of zero strain. Peak acceleration of the distension waveform on the phantom wall was used to track the pulse wave velocity. Both FSI simulations and experiments showed good agreement in quantifying the plaque stiffness based on the PWV, whereas stiffer plaque showed larger PWV in both FSI simulations and experiments. PWVs of 2.57 ms^{-1}, 3.41 ms^{-1}, and 4.48 ms^{-1} were found for plaque materials with soft, intermediate, and stiff constituents using PWI in phantoms. PWVs of 2.10 ms^{-1}, 3.33 ms^{-1}, and 4.02 ms^{-1} were respectively found for soft, intermediate, and stiff plaque constituents in FSI simulations. These results demonstrate that PWI can effectively distinguish the mechanical properties of plaque in phantoms.

CRediT authorship contribution statement

Nima Mobadersany: Writing – original draft, Visualization, Validation, Software, Methodology, Investigation, Formal analysis, Data curation, Conceptualization. **Nirvedh H. Meshram:** Validation, Methodology, Investigation, Formal analysis, Data curation. **Paul Kemper:** Writing – review & editing, Methodology, Formal analysis. **C.V. Sise:** Resources, Methodology, Investigation. **Grigorios M. Karageorgos:** Writing – review & editing, Methodology. **Pengcheng Liang:** Writing –

review & editing, Methodology. **Gerard A. Ateshian:** Writing – review & editing, Software, Resources, Methodology. **Elisa E. Konofagou:** Writing – review & editing, Supervision, Resources, Project administration, Methodology, Funding acquisition, Conceptualization.

Declaration of Competing Interest

The authors declare that they have no known competing financial interests or personal relationships that could have appeared to influence the work reported in this paper.

Acknowledgments

The authors gratefully acknowledge the funding from the National Institutes of Health (5R01HL135734) to support this work. The authors thank Jay J. Shim, Ph.D., for helpful discussions and Pablo Abreu, M.S. for administrative assistance.

Appendix A

Ultrasound acquisitions were carried out along the longitudinal axis of the phantom by using a coherent compounding sequence involving transmission of 3 plane waves at angles of ($-2^{\circ}, 0^{\circ}, 2^{\circ}$), at a pulse repetition frequency of 8333 Hz (Apostolakis et al., 2017). Channel data were recorded over a time interval of 1 s, and the acquisition sequence was synchronized with the beginning of the pump cycle by using an artificial ECG trigger provided by the pump. The radio frequency (RF) data were beamformed using the delay and sum algorithm and then coherently summed, producing thus compounded RF frames of improved quality with an effective frame rate of 2777 Hz. A graphics processing unit accelerated 1D cross-correlation method (Luo and Konofagou, 2010) was used to estimate the incremental axial displacements among consecutive frames, which were then normalized with the frame rate to generate axial wall velocities. To estimate the wall motion, the interior of the upper and lower walls of the phantom and plaque were segmented to obtain the temporal waveform of the axial wall velocities at each lateral location. The upper wall velocity was subtracted from that of the lower wall to eliminate any rigid motion and obtain a spatiotemporal map of the axial distension rate of the phantom, to visualize the pulse wave propagation. Subsequently, the axial distension rate was filtered with a 3x3 median kernel and then temporally differentiated to obtain the distension acceleration (Karageorgos et al., 2020).

Appendix B

Mechanical properties of the plaque material, phantom wall, and surrounding gelatin were measured using unconfined compression stress-relaxation tests performed on the cubic samples that were constructed with identical protocols as the PVA phantoms. Each cubic sample was subjected to a linearly increasing compressive displacement from zero to 15% engineering strain, then maintained constant for 3000 s. The engineering stress response (force divided by initial cross-sectional area) was recorded and analyzed to obtain the viscoelastic properties of the phantom materials.

Appendix C

Several markers have already been proposed to track the pulse wave arrival time, i.e., 50% upstroke of the velocity waveform (defined as the time-point corresponding to the middle of the foot and the peak of the phantom wall distension rate, so that the forward wave is less affected by the generated reflected wave (Apostolakis et al., 2017; Nichols et al., 2011)), and the peak of the acceleration distension waveform. To apply the more reliable PWV marker for this study, pulse wave velocity was first found on the straight phantom using PWI to confirm the expected pulse wave velocity value at the pre-stenosis region. Fig. C1 (a) shows the mapping of PWV on the spatiotemporal map of the axial distension rate in the straight phantom across the field of view. Fig. C1 (b-c) shows the PWV in the pre-stenosis region of the stenotic phantom with two different markers to track the pulse wave arrival time: 50% upstroke of the velocity waveform and peak acceleration waveform, respectively. The start of the stenosis is marked with dashed line on the spatiotemporal map and is located at around 0.065 m away from the phantom inlet. The small circles overlaid on the maps indicate the marker arrival time with the corresponding linear fitting. At regions further away from the plaque, both markers provide similar PWV values like that observed in straight phantom.

However, unlike the peak acceleration marker, tracking 50% upstroke of velocity waveform overestimates the PWV at the pre-stenosis region by the plaque. This overestimation in PWV is due to the reflections from the plaque that interferes with the forward pulse wave. Since acceleration waveform has higher frequency components and lower periods, it provides better separation of the forward and reflected pulse wave, as it is observed in Fig. C2. Note that shorter pulse waves would provide better estimation of pulse wave arrival time. Shorter pulse waves have shorter periods, thus resulting in less interference between the forward and reflected waves.

On the other hand, the reflections of shorter pulse waves would attenuate more due to their higher frequency, potentially reducing the effect of reflections on pulse wave arrival time estimation. In this study, we have followed a similar rationale to estimate pulse wave arrival time by monitoring wall distension acceleration waveform rather than the wall distension rate. It is because the distension acceleration waveform has a higher frequency, resulting in better separation of forward and reflected waves. Fig. C2 shows the spatiotemporal map of (a) axial wall distension rate, and (b) axial wall distension acceleration at the pre-stenosis of the stenotic phantom experiment. As noted, wall acceleration provides better separation of the forward and reflected pulse wave. Therefore, tracking peak distension acceleration of the wall provides more reliable PWV estimation at the stenotic region. Therefore, it has been used as the wave arrival time marker in this study.

Appendix D

As a reference, the PWV at the stenosis of three phantoms (with 50% stenosis degree) in another case study was shown in figure D (Mobadersany et al., 2023) which was found by PWI. One objective of this case study (Mobadersany et al., 2023) was to evaluate the capability of PWI in assessing plaque heterogeneity where both softer and stiffer constituents are present in each plaque. As part of the case study, three PVA stenotic phantoms (50% stenosis degree) with homogeneous plaque constituents of soft, intermediate, and stiff were constructed along with the heterogeneous plaques for comparison. For constructing the phantoms, the PVA solution was prepared following the similar procedure discussed earlier. However, the number of freezing and thawing cycles were modulated during the fabrication process to generate soft (E0 = 13 kPa), intermediate (E0 = 40 kPa), and stiff (E0 =

54 kPa) constituents with the phantom wall having the same mechanical properties as the intermediate constituent.

Fig. D1 shows the spatiotemporal map and PWV of these homogeneous soft, intermediate, and stiff plaques. However, the spatiotemporal map and PWV of the heterogeneous plaques have not been provided here since the plaque heterogeneity is not the scope of the current study. As shown in figure D, pulse wave velocities of 2.06 ms-1, 2.49 ms-1, and 3.31 ms-1 were found using PWI for soft plaque, intermediate plaque, and stiff plaque, respectively in this set of phantoms with the stiffer plaque showing larger PWV values, and lower distension rate.

References

Ahmadi, M., Ansari, R., 2019. Computational simulation of an artery narrowed by plaque using 3D FSI method: Influence of the plaque angle, non-Newtonian properties of the blood flow and the hyperelastic artery models. Biomed. Phys. Eng. Express 5, 045037. https://doi.org/10.1088/2057-1976/ab323f.

Apostolakis, I.Z., Mcgarry, M.D.J., Bunting, E.A., Konofagou, E.E., 2017. Pulse wave imaging using coherent compounding in a phantom and in vivo. Phys. Med. Biol. 62, 1700–1730. https://doi.org/10.1088/1361-6560/aa553a.

Bazilevs, Y., Calo, V.M., Zhang, Y., Hughes, T.J.R., 2006. Isogeometric fluid-structure interaction analysis with applications to arterial blood flow. Comput. Mech. 38, 310–322. https://doi.org/10.1007/s00466-006-0084-3.

Bennati, L., Vergara, C., Domanin, M., Malloggi, C., Bissacco, D., Trimarchi, S., Silani, V., Parati, G., Casana, R., 2021. A Computational Fluid-Structure Interaction Study for Carotids With Different Atherosclerotic Plaques. J. Biomech. Eng. 143, 1–15. https://doi.org/10.1115/1.4050910.

Blacher, J., Fournier, V., Asmar, R., Guerin, A.P., Pannier, B., Safar, M.E., London, G.M., 2001. Aortic pulse wave velocity as a marker of atherosclerosis in hypertension. Cardiovasc. Rev. Reports 22, 420-425+431.

Blacher, J., Safar, M.E., Guerin, A.P., Pannier, B., Marchais, S.J., London, G.M., 2003. Aortic pulse wave velocity index and mortality in end-stage renal disease. Kidney Int. 63, 1852–1860. https://doi.org/10.1046/j.1523-1755.2003.00932.x.

Bluestein, D., Gutierrez, C., Londono, M., Schoephoerster, R.T., 1999. Vortex Shedding in Steady Flow Through a Model of an Arterial Stenosis and Its Relevance to Mural Platelet Deposition. Ann. Biomed. Eng. 27, 763–773. https://doi.org/10.1114/1.230.

Chayer, B., van den Hoven, M., Cardinal, M.-H.-R., Li, H., Swillens, A., Lopata, R., Cloutier, G., 2019. Atherosclerotic carotid bifurcation phantoms with stenotic soft inclusions for ultrasound flow and vessel wall elastography imaging. Phys. Med. Biol. 64, 095025 https://doi.org/10.1088/1361-6560/ab1145.

Chee, A.J.Y., Ho, C.K., Yiu, B.Y.S., Yu, A.C.H., 2016. Walled Carotid Bifurcation Phantoms for Imaging Investigations of Vessel Wall Motion and Blood Flow Dynamics. IEEE Trans. Ultrason. Ferroelectr. Freq. Control 63, 1852–1864. https://doi.org/10.1109/TUFFC.2016.2591946.

Chiha, J., Mitchell, P., Gopinath, B., Burlutsky, G., Plant, A., Kovoor, P., Thiagalingam, A., 2016. Prediction of coronary artery disease extent and severity using pulse wave velocity. PLoS One 11, 1–10. https://doi.org/10.1371/journal.pone.0168598.

Cicha, I., Wörner, A., Urschel, K., Beronov, K., Goppelt-Struebe, M., Verhoeven, E., Daniel, W.G., Garlichs, C.D., 2011. Carotid plaque vulnerability: a positive feedback between hemodynamic and biochemical mechanisms. Stroke 42, 3502–3510. https://doi.org/10.1161/STROKEAHA.111.627265.

Couade, M., Pernot, M., Messas, E., Emmerich, J., Hagège, A., Fink, M., Tanter, M., 2011. Ultrafast imaging of the arterial pulse wave. IRBM 32, 106–108. https://doi.org/10.1016/j.irbm.2011.01.012.

Czernuszewicz, T.J., Homeister, J.W., Caughey, M.C., Farber, M.A., Fulton, J.J., Ford, P. F., Marston, W.A., Vallabhaneni, R., Nichols, T.C., Gallippi, C.M., 2015. Non-invasive in vivo characterization of human carotid plaques with acoustic radiation force impulse ultrasound: Comparison with histology after endarterectomy. Ultrasound Med. Biol. 41, 685–697. https://doi.org/10.1016/j.ultrasmedbio.2014.09.016.

Donnan, G.A., Fisher, M., Macleod, M., Davis, S.M., 2008. Stroke. Lancet 371, 1612–1623. https://doi.org/10.1016/S0140-6736(08)60694-7.

Elkenani, H., Al-Bahkali, E., Souli, M., 2017. Numerical Investigation of Pulse Wave Propagation in Arteries Using Fluid Structure Interaction Capabilities. Comput. Math. Methods Med. 2017 https://doi.org/10.1155/2017/4198095.

Fujikura, K., Luo, J., Gamarnik, V., Pernot, M., Fukumoto, R., Tilson, M.D., Konofagou, E. E., 2007. A novel noninvasive technique for pulse-wave imaging and characterization of clinically-significant vascular mechanical properties in vivo. Ultrason. Imaging 29, 137–154. https://doi.org/10.1177/016173460702900301.

Galluzzo, F., Leonardo, F., Ceruti, A., De Marchi, L., Corsi, C., 2015. Design of anthropomorphic atherosclerotic carotid artery flow phantoms for ultrasound images. Comput. Cardiol. (2010). 42, 721–724. https://doi.org/10.1109/CIC.2015.7411012.

Gatti, V., Nauleau, P., Karageorgos, G.M., Shim, J.J., Ateshian, G.A., Konofagou, E.E., 2020. Modeling Pulse Wave Propagation Through a Stenotic Artery With Fluid Structure Interaction: A Validation Study Using Ultrasound Pulse Wave Imaging. J. Biomech. Eng. 143, 1–11. https://doi.org/10.1115/1.4048708.

Hafiane, A., 2019. Vulnerable Plaque, Characteristics, Detection, and Potential Therapies. J. Cardiovasc. Dev. Dis. 6, 26. https://doi.org/10.3390/jcdd6030026.

Holdsworth, D.W., Norley, C.J.D., Frayne, R., Steinman, D.A., Rutt, B.K., 1999. Characterization of common carotid artery blood-flow waveforms in normal human subjects. Physiol. Meas. 20, 219–240. https://doi.org/10.1088/0967-3334/20/3/301.

Luo, J., Konofagou, E.E., 2010. A fast normalized cross-correlation calculation method for motion estimation. IEEE Trans. Ultrason. Ferroelectr. Freq. Control 57, 1347–1357. https://doi.org/10.1109/TUFFC.2010.1554.

Karageorgos, G.M., Apostolakis, I.-Z., Nauleau, P., Gatti, V., Weber, R., Kemper, P., Konofagou, E.E., 2021. Pulse Wave Imaging Coupled With Vector Flow Mapping: A Phantom, Simulation, and In Vivo Study. IEEE Trans. Ultrason. Ferroelectr. Freq. Control 68, 2516–2531. https://doi.org/10.1109/TUFFC.2021.3074113.

Karageorgos, G.M., Apostolakis, I.Z., Nauleau, P., Gatti, V., Weber, R., Connolly, E.S., Miller, E.C., Konofagou, E.E., 2020. Arterial wall mechanical inhomogeneity detection and atherosclerotic plaque characterization using high frame rate pulse wave imaging in carotid artery disease patients in vivo. Phys. Med. Biol. 65, 025010 https://doi.org/10.1088/1361-6560/ab58fa.

Karageorgos, G.M., Kemper, P., Lee, C., Weber, R., Kwon, N., Meshram, N., Mobadersany, N., Grondin, J., Marshall, R.S., Miller, E.C., Konofagou, E.E., 2022. Adaptive Wall Shear Stress Imaging in Phantoms, Simulations and in Vivo. IEEE Trans. Biomed. Eng. PP, 1–12. https://doi.org/10.1109/TBME.2022.3186854.

Kim, B.H., Jang, J.S., Kwon, Y.S., Kim, J.H., Kim, I.J., Lee, C.W., 2018. High Brachial Ankle Pulse Wave Velocity as a Marker for Predicting Coronary Artery Stenosis in Patients with Type 2 Diabetes. Endocrinol Metab 33, 88–96. https://doi.org/10.3803/EnM.2018.33.1.88.

Kim, H.L., Kim, S.H., 2019. Pulse Wave Velocity in Atherosclerosis. Front. Cardiovasc. Med. 6, 1–13. https://doi.org/10.3389/fcvm.2019.00041.

Lechareas, S., Yanni, A.E., Golemati, S., Chatziioannou, A., Perrea, D., 2016. Ultrasound and Biochemical Diagnostic Tools for the Characterization of Vulnerable Carotid Atherosclerotic Plaque. Ultrasound Med. Biol. 42, 31–43. https://doi.org/10.1016/j.ultrasmedbio.2015.09.003.

Li, R.X., Apostolakis, I.Z., Kemper, P., McGarry, M.D.J.J., Ip, A., Connolly, E.S., McKinsey, J.F., Konofagou, E.E., 2019. Pulse Wave Imaging in Carotid Artery Stenosis Human Patients in Vivo. Ultrasound Med. Biol. 45, 353–366. https://doi.org/10.1016/j.ultrasmedbio.2018.07.013.

Lim, H.E., Park, C.G., Shin, S.H., Ahn, J.C., Seo, H.S., Oh, D.J., 2004. Aortic pulse wave velocity as an independent marker of coronary artery disease. Blood Press. 13, 369–375. https://doi.org/10.1080/08037050410004800.

Liu, X.N., Gao, H.Q., Li, B.Y., Cheng, M., Ma, Y.B., Zhang, Z.M., Gao, X.M., Liu, Y.P., Wang, M., 2007. Pulse wave velocity as a marker of a arteriosclerosis and its comorbidities in Chinese patients. Hypertens. Res. 30, 237–242. https://doi.org/10.1291/hypres.30.237.

Maas, S.A., Ellis, B.J., Ateshian, G.A., Weiss, J.A., 2012. FEBio: finite elements for biomechanics. J. Biomech. Eng. 134, 011005 https://doi.org/10.1115/1.4005694.

Majdouline, Y., Ohayon, J., Keshavarz-Motamed, Z., Roy Cardinal, M.H., Garcia, D., Allard, L., Lerouge, S., Arsenault, F., Soulez, G., Cloutier, G., 2014. Endovascular shear strain elastography for the detection and characterization of the severity of atherosclerotic plaques: In vitro validation and in vivo evaluation. Ultrasound Med. Biol. 40, 890–903. https://doi.org/10.1016/j.ultrasmedbio.2013.12.008.

Marlevi, D., Mulvagh, S.L., Huang, R., DeMarco, J.K., Ota, H., Huston, J., Winter, R., Macedo, T.A., Abdelmoneim, S.S., Larsson, M., Pellikka, P.A., Urban, M.W., 2020. Combined spatiotemporal and frequency-dependent shear wave elastography enables detection of vulnerable carotid plaques as validated by MRI. Sci. Rep. 10, 403. https://doi.org/10.1038/s41598-019-57317-7.

Mobadersany, N., Liang, P., Kemper, P., Konofagou, E.E., 2023. PVA Phantoms with Heterogeneous Plaques: Investigation of Pulse Wave Velocity at the Stenotic Region using Pulse Wave Imaging. Journal of. Ultrasound in Medicine and Biology. Submitted.

Nichols, W.W., O'Rourke, M.F., Vlachopoulos, C., Hoeks, A.P., Reneman, R.S., 2011. McDonald's blood flow in arteries theoretical, experimental and clinical principles, McDonald's Blood Flow in Arteries, Sixth Edition: Theoretical, Experimental and Clinical Principles. Hodder Arnold ; Distributed in the U.S.A. by Oxford University Press, London; New York. https://doi.org/10.1111/j.1540-8175.1991.tb01207.x.

Paley, M., Hose, R., Marzouqa, I., Fenner, J., Wilkinson, I., Noguchi, Y., Griffiths, P., 2000. Stable periodic vortex shedding studied using computational fluid dynamics, laser sheet flow visualization, and MR imaging. Magn. Reson. Imaging 18, 473–478. https://doi.org/10.1016/S0730-725X(99)00136-8.

Patel, M., Savvopoulos, F., Berggren, C.C., Aslanidou, L., Timmins, L.H., de Silva, R., Pedrigi, R.M., Krams, R., 2021. Considerations for analysis of endothelial shear stress and strain in FSI models of atherosclerosis. J. Biomech. 128, 1–9. https://doi.org/10.1016/j.jbiomech.2021.110720.

Ramnarine, K.V., Nassiri, D.K., Hoskins, P.R., Lubbers, J., 1998. Validation of a new blood-mimicking fluid for use in Doppler flow test objects. Ultrasound Med. Biol. 24, 451–459. https://doi.org/10.1016/s0301-5629(97)00277-9.

Saba, L., Anzidei, M., Marincola, B.C., Piga, M., Raz, E., Bassareo, P.P., Napoli, A., Mannelli, L., Catalano, C., Wintermark, M., 2014. Imaging of the carotid artery vulnerable plaque. Cardiovasc. Intervent. Radiol. 37, 572–585. https://doi.org/10.1007/s00270-013-0711-2.

Scuteri, A., Wang, H., 2014. Pulse wave velocity as a marker of cognitive impairment in the elderly. J. Alzheimer's Dis. 42, S401–S410. https://doi.org/10.3233/JAD-141416.

Shahmirzadi, D., Li, R.X., Konofagou, E.E., 2012. Pulse-Wave Propagation in Straight-Geometry Vessels for Stiffness Estimation: Theory, Simulations, Phantoms and In Vitro Findings. J. Biomech. Eng. 134, 1–6. https://doi.org/10.1115/1.4007747.

Shim, J.J., Maas, S.A., Weiss, J.A., Ateshian, G.A., 2021. Finite Element Implementation of Biphasic-Fluid Structure Interactions in febio. J. Biomech. Eng. 143 https://doi.org/10.1115/1.4050646.

Shim, J.J., Maas, S.A., Weiss, J.A., Ateshian, G.A., 2019. A Formulation for Fluid-Structure Interactions in FEBIO Using Mixture Theory. J. Biomech. Eng. 141, 1–15. https://doi.org/10.1115/1.4043031.

Spronck, B., Heusinkveld, M.H.G., Vanmolkot, F.H., Roodt, J.O. t., Hermeling, E., Delhaas, T., Kroon, A.A., Reesink, K.D., 2015. Pressure-dependence of arterial stiffness: potential clinical implications. J. Hypertens. 33, 330–8. https://doi.org/10.1097/HJH.0000000000000407.

Surry, K.J.M., Austin, H.J.B., Fenster, A., Peters, T.M., 2004. Poly(vinyl alcohol) cryogel phantoms for use in ultrasound and MR imaging. Phys. Med. Biol. 49, 5529–5546. https://doi.org/10.1088/0031-9155/49/24/009.

Tang, D., Yang, C., Zheng, J., Woodard, P.K., Saffitz, J.E., Sicard, G.A., Pilgram, T.K., Yuan, C., 2005. Quantifying effects of plaque structure and material properties on stress distributions in human atherosclerotic plaques using 3D FSI models. J. Biomech. Eng. 127, 1185–1194. https://doi.org/10.1115/1.2073668.

Vappou, J., Luo, J., Konofagou, E.E., 2010. Pulse Wave Imaging for Noninvasive and Quantitative Measurement of Arterial Stiffness In Vivo. Am. J. Hypertens. 23, 393–398. https://doi.org/10.1038/ajh.2009.272.

Widman, E., Maksuti, E., Larsson, D., Urban, M.W., Bjällmark, A., Larsson, M., 2015. Shear wave elastography plaque characterization with mechanical testing validation: A phantom study. Phys. Med. Biol. 60, 3151–3174. https://doi.org/10.1088/0031-9155/60/8/3151.

Wong, K.K., Thavornpattanapong, P., Cheung, S.C., Sun, Z., Tu, J., 2012. Effect of calcification on the mechanical stability of plaque based on a three-dimensional carotid bifurcation model. BMC Cardiovasc. Disord. 12, 7. https://doi.org/10.1186/1471-2261-12-7.

Wu, M., Awasthi, N., Rad, N.M., Pluim, J.P.W., Lopata, R.G.P., 2021. Advanced Ultrasound and Photoacoustic Imaging in Cardiology. Sensors (Basel). 21, 7947. https://doi.org/10.3390/s21237947.

Yuan, J., Teng, Z., Feng, J., Zhang, Y., Brown, A.J., Gillard, J.H., Jing, Z., Lu, Q., 2015. Influence of material property variability on the mechanical behaviour of carotid atherosclerotic plaques: A 3D fluid-structure interaction analysis. Int. j. numer. method. biomed. eng. 31, 1–12. https://doi.org/10.1002/cnm.2722.

Zhai, F.-F.-F., Ye, Y.-C.-C., Chen, S.-Y.-Y., Ding, F.-M.-M., Han, F., Yang, X.-L.-L., Wang, Q., Zhou, L.-X.-X., Ni, J., Yao, M., Li, M.-L.-L., Jin, Z.-Y.-Y., Cui, L.-Y.-Y., Zhang, S.-Y.-Y., Zhu, Y.-C.-C., 2018. Arterial Stiffness and Cerebral Small Vessel Disease. Front. Neurol. 9, 1–7. https://doi.org/10.3389/fneur.2018.00723.

Zhou, H., Meng, L., Zhou, W., Xin, L., Xia, X., Li, S., Zheng, H., Niu, L., 2017. Computational and experimental assessment of influences of hemodynamic shear stress on carotid plaque. Biomed. Eng. Online 16, 92. https://doi.org/10.1186/s12938-017-0386-z.

Zureik, M., Temmar, M., Adamopoulos, C., Bureau, J.-M.-M., Courbon, D., Thomas, F., Bean, K., Touboul, P.-J.-J., Ducimetière, P., Benetos, A., 2002. Carotid plaques, but not common carotid intima–media thickness, are independently associated with aortic stiffness. J. Hypertens. 20, 85–93. https://doi.org/10.1097/00004872-200201000-00013.